Optical and Quantum Electronics (2021) 53:197
https://doi.org/10.1007/s11082-021-02851-w

Investigation of amorphous-crystalline transformation induced optical and electronic properties change in annealed $As_{50}Se_{50}$ thin films

D. Sahoo[1] · P. Priyadarshini[1] · R. Dandela[2] · D. Alagarasan[3] · R. Ganesan[3] · S. Varadharajaperumal[4] · Ramakanta Naik[1]

Received: 12 November 2020 / Accepted: 29 March 2021 / Published online: 3 April 2021
© The Author(s), under exclusive licence to Springer Science+Business Media, LLC, part of Springer Nature 2021

Abstract
The present work reports the amorphous-crystalline phase transformation in thermally evaporated $As_{50}Se_{50}$ thin films upon annealing at below T_g (423 K) and above T_g (523 K). The structural transition was probed by XRD, Raman and X-ray photoelectron spectroscopy. The composition and surface morphology were probed by EDS and FESEM techniques. The transmittance and reflectance spectra over the wavelength range 500 nm–1200 nm were used to deduce the optical parameters. The various optical parameters of the as-prepared and annealed $As_{50}Se_{50}$ thin films were estimated and discussed in terms of density of defect states and disorders. The indirect optical energy gap decreased for the 423 K annealed film and abruptly increased for 523 K annealed film as compared to the as-prepared film. The Swanepoel envelope method, WDD model, and Sellemeire postulates were employed for the analysis of refractive index, static refractive index, oscillator energy, dispersion energy, oscillator wavelength and dielectric constant. The changes in the linear and nonlinear properties showed opposite behavior for the two annealed films. The non-linear refractive index and 3rd order susceptibility were found to be increased for 423 K annealed film and decreased for the 523 K annealed film. The optical as well as the electrical conductivity changed with annealing and the electrical susceptibility increased for 523 K annealed film. The tunable optical properties can be applied for several optoelectronic applications.

✉ Ramakanta Naik
ramakanta.naik@gmail.com

1 Department of Engineering and Material Physics, ICT-IOC, Bhubaneswar 751013, India

2 Department of Industrial and Engineering Chemistry, ICT-IOC, Bhubaneswar 751013, India

3 Department of Physics, Indian Institute of Science, Bangalore 560012, India

4 Centre for Nano Science and Engineering, Indian Institute of Science, Bangalore 560012, India

Graphical abstract

The amorphous to crystalline structural transformation occurred at annealing above Tg. The 3rd order susceptibility was found to be more at 423 K annealing and less at 523 K annealing.

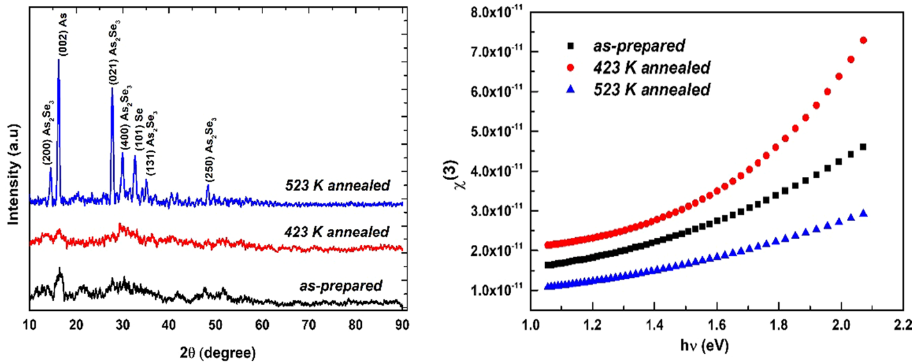

Keywords Thin films · Annealing · Optical parameter · Refractive index · Nonlinear refractive index · 3rd order nonlinear susceptibility

1 Introduction

The amorphous to crystalline transition in amorphous chalcogenides forms the basis of information encoding used for rewritable discs (Zhang et al. 2019). The peculiar sensitive property of amorphous-crystalline and reversible phase transformation makes it suitable for optical recording medium (Frumar et al. 2007). The most disorder state to order state transition suits these materials for high resolution display and high-density information storage devices (Ovshinisky and Fritzsche 1973). Such chalcogenide materials are defined as a type of amorphous isotropic one having glass transition and relaxation time ~ 10^3 s (Tammama et al. 2020). They are basically in non-equilibrium state in their as-prepared condition due to the sudden quenching process (Nordman et al. 1998). The various characteristic parameters should be in their stable form while using them for various applications which can be done by thermal annealing at different temperatures (Sahoo et al. 2020a), bombarding with energetic ions (Behera et al. 2020), laser irradiation (Aparimita et al. 2020a), gamma and X-ray irradiation (Sharma et al. 2020) and many other suitable techniques. The chalcogenide thin films switched locally by means of structural, optical and electrical parameters upon such treatments and found important applications in optoelectronic devices, solar cells, infrared detectors, optical biosensors, low loss waveguides, optical switches, fibers and many more (Manivannan and Noyel Victoria 2018; Purohit et al. 2015; Xu et al. 2014; Zhai et al. 2016; Anne et al. 2009; Sojka et al. 2012). The reason behind such numerous applications of these materials lies in their linear-nonlinear optical, thermal, structural, electrical properties like high IR transmission, low phonon energy, large nonlinear susceptibility etc. (Eggleton et al. 2011; Zakery and Elliott 2003). The chalcogenide films have large nonlinear optical behaviour than the oxide counterpart due to the presence of heavy chalcogen atoms that have vibrational bonding at low energy. Among these, Se based films show high transparency, strong non-linear properties and reversible

phase transformation (Lencer et al. 2008). In particular, As-Se alloys have found significant applications due to their large change in nonlinear as well as linear optical properties because of the available double lone pair electrons (Adam and Zhang 2013).

Thermal annealing on the films plays an important role in modifying their structural, morphological and optical properties. The selection of the annealing temperature depends on the characteristic glass transition temperature (T_g) and crystallization temperature (T_c) of that particular material. The T_g is the lower limit for inducing crystallization after which the amorphous material starts to crystallize (Tripathi et al. 2016). The reduction in structural defects and increase in crystallinity upon amorphous-crystalline phase transformation by thermal annealing resulted strong optical and structural changes in such films (Darwish and Ali 2017). The changes in various properties like the decrease in E_{opt} by annealing due to phase transition in $Se_{85}In_{15-x}Zn_x$ thin films is an important feature specifically for optical recording memory (Srivastava et al. 2018). The electrical conductivity and optical bandgap tuning in $Bi_xIn_{25-x}Se_{75}$ films on annealing caused due to phase reversal phenomena (Sharma et al. 2013). The optical reflectivity and creation of rippled surface occurred upon annealing near T_g in the As-Se film that depends on the As concentration (Tsvetkova et al. 2004). Similarly, the increase in annealing temperature with duration leads to the transformation of structural properties by the formation of $AsSe_3$ pyramidal units with low surface roughness (Zou et al. 2012). Annealing near T_g results in the polymerization of the structure through the conversion of homopolar bonds to heteropolar bonds. The linear optical properties of As_2Se_3 was increased due to annealing near its T_{g} (Charlie et al. 2011). The annealing of $As_{50}Se_{50}$ film at temperature 423 K (near its T_g) enhanced the concentration of heteropolar bonds over homopolar ones thus making it more homogeneous surface (Siokou et al. 2006). The thermal annealing reduced the structural and electronic defects in the PLD based $As_{50}Se_{50}$ films (Kalyva et al. 2007). The lack of systematic study on the tailoring of the nonlinear and linear optical properties of $As_{50}Se_{50}$ film by annealing below and above T_g encouraged us for the present study.

The present study is focused on the analysis of both nonlinear and linear optical parameters of $As_{50}Se_{50}$ thin film annealed at both below and above its T_g that caused amorphous-crystalline phase transformation. The annealing was done at 423 K (below T_g) and 523 K (above T_g) on the thermally evaporated $As_{50}Se_{50}$ film. The X-ray diffraction (XRD), Raman spectroscopy were done for structural investigation while UV–Visible spectroscopy was done for optical property study. The obtained linear parameters were used to derive the nonlinear constants by using the semi empirical Miller's formula. The various linear and nonlinear optical parameters were calculated for these two annealed films and compared with the as-prepared one.

2 Experimental work

2.1 Sample preparation

The bulk $As_{50}Se_{50}$ sample was prepared by conventional melt quenching method by mixing high purity (99.999% Sigma Aldrich) As and Se elements at proper stoichiometric amount in a quartz ampoule. The ampoule was sealed under high vacuum and put inside the furnace which was under a temperature of 900 °C at the heating rate of 3°–4° C/min. The 900 °C condition was maintained for 24 h. The ampules were constantly shaken during heating in order to get a homogeneous mixture. The rapid quenching of the melt was done in ice-cold water and the

bulk $As_{50}Se_{50}$ sample was collected after breaking the quenched ampoule. The thin film was prepared on the glass substrate from the bulk $As_{50}Se_{50}$ sample in thermal evaporation method by using the vacuum coating unit (HIND-HIVAC Model 12A4D). The evaporation was done at room temperature with an evaporation rate of 5 Å/s at a vacuum of 2×10^{-5} Torr. The film thickness was ~ 800 nm as observed from the attached quartz crystal monitor. The as-prepared thin film was annealed at 423 K (below T_g) and 523 K (above T_g) respectively for 2 h.

2.2 Experimental techniques

In order to investigate the structural transformation due to annealing, the XRD was done for the as-prepared and annealed films by Cu-Kα radiation (λ = 1.54 Å) in Bruker D8 Advance machine. The data were recorded with a scan speed of 1° min^{-1}, a step value of 0.02° in 2θ range of 10°–90° at a grazing angle of 1°. The Raman spectroscopy was done (LabRAM HR system) by 514.5 nm argon laser with a CCD detector in backscattering mode in the range of 50 cm^{-1}–400 cm^{-1}. The presence of constituent elements such as As and Se was checked by Energy-dispersive X-ray analysis (EDS) and corresponding surface morphology of the films was taken by Field emission scanning electron microscope (FESEM). The scanning was done for 1 cm^2 film area size by 20 kV voltage and 40 mA emission current at a pressure of 2×10^{-7} Torr. The data was taken 3–4 times at different portions of the film to minimize the errors. The optical analysis was done from the reflectance and transmittance data recorded by UV–Vis Spectrometer (IFS66v/S) in 500 nm–1200 nm wavelength range at room temperature. The information about different chemical bonding modifications in the as-prepared and annealed film was recorded in X-ray photoelectron spectroscopy (XPS) (Axis Ultra, Kratos Analytical, UK) measurement. The required core level XPS spectra were taken by Al K_α X-rays (1486.6 eV) under a vacuum of 2×10^{-9} Torr. Due to the insulating nature of the prepared glassy films, the required charge correction was done with the recorded C1s binding energy (BE) as compared to the standard C1s of 284.6 eV (Barr and Seal 1995; Naik et al. 2009). The original BE data correction was done by using the calibration factor. The scan was performed at different positions of the films to reproduce the data.

3 Results and discussion

3.1 Structural analysis

3.1.1 (a) XRD study

The as-prepared and 423 K annealed $As_{50}Se_{50}$ film showed amorphous structure as shown in Fig. 1. The small humps appeared at different θ values are due to the glass substrates used for film preparation (Pradhan et al. 2018). However, when the film was annealed at 523 K, the corresponding structure transformed from amorphous to crystalline as shown in Fig. 1. The phases like As_2Se_3, As, Se grown upon annealing above T_g and the crystallite size (D_{hkl}) was estimated using the well-known Scherrer's equation (Patterson 1939)

$$\text{Crystallite size } (D) = \frac{0.9\lambda}{\beta\cos\theta}(\beta \text{ in radian}) \tag{1}$$

where λ, β, θ are the wavelength of Cu Kα (1.54 Å), Full width half maxima (FWHM) and Bragg angle respectively. The calculated crystallite sizes of different phases are presented

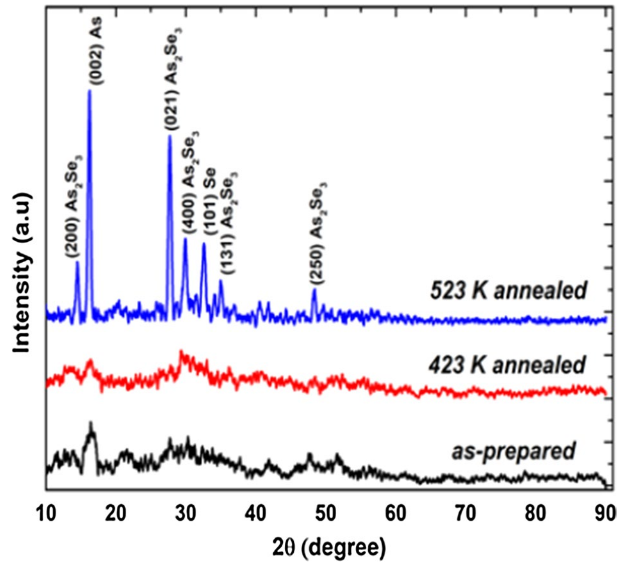

Fig. 1 XRD patterns of the as-prepared and annealed thin films

in Table 1. It was observed that the film structure was maximum converted into As_2Se_3 phase whose average crystallite size becomes 20.43 nm upon annealing above T_g.

The dislocation density (δ) which is defined as the length of the dislocation lines per unit volume of the crystal (Aparimita et al. 2020b), the lattice strain of the different phases (ϵ) and number of crystallites per unit surface area (N) were evaluated and presented in Table 1 (Abd-Elnaiem et al. 2020a).

3.2 (b) Raman analysis

Figure 2 presents the Raman spectra for the as-prepared and annealed films that show peaks at different wavenumbers. The peak located at 221 cm^{-1} is due to the As-Se vibration of pyramidal $AsSe_{3/2}$ symmetric stretching units (Němec et al. 2005). However, there is a shoulder peak at 241 cm^{-1} which is assigned to the vibrations of AsSe structural units (Kudryashov et al. 2019). The intensity of these two peaks increased for the 423 K

Table 1 XRD parameters for the 523 K annealed film

2θ	Phase	hkl Plane	Crystallite size (D) in nm	Dislocation density $(\delta)\times 10^{15}(/m^2)$	Strain $(\varepsilon)\times 10^{-4}$	N($/nm^2$)
14.48	As_2Se_3	(200)	19.51	2.627	2.377	0.108
16.21	As	(0 0 2)	18.7	2.859	2.850	0.122
27.72	As_2Se_3	(0 2 1)	18	3.086	5.181	0.137
29.94	As_2Se_3	(4 0 0)	19.2	2.712	5.792	0.113
32.61	Se	(1 0 1)	15.4	4.216	6.708	0.219
35.01	As_2Se_3	(1 3 1)	23.31	1.841	5.140	0.063
48.35	As_2Se_3	(2 5 0)	22.13	2.041	8.053	0.073

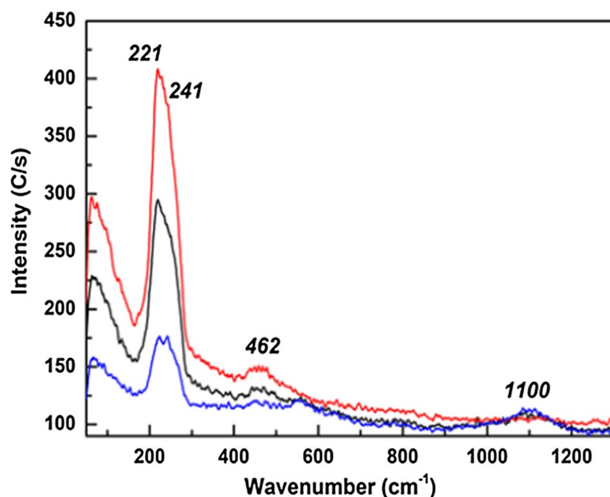

Fig. 2 Raman spectra of the as-prepared and annealed thin films

annealed film while it decreased for the 523 K annealed film. Also, the position of these peaks shifted upon annealing which confirms the structural transition due to annealing at below and above T_g. There is another low intensity peak at 462 cm^{-1} which may be for Se-Se vibrational bonds whose intensity increased for 423 K annealed film while it disappeared at 523 K annealing. Similarly, the low intensity peak appeared at 1100 cm^{-1} disappeared for 423 K annealing but developed for the 523 K annealing.

4 Composition and surface morphology study

The constituent As and Se elements of both as-prepared and annealed films was verified by EDS picture as shown in Fig. 3. The respective peaks correspond to different elements and the corresponding film composition is approximately same and within 4% error as compared to the calculated value as given in Table 2.

The FESEM pictures taken at 200 nm scale for the as-prepared and annealed $As_{50}Se_{50}$ thin films are shown in Fig. 4. The pictures show the homogeneous and smooth nature of the films. The annealing induced phase transformation is visible in FESEM images in which amorphous like surface was observed in the 423 K annealed film and appearance of crystallites in the 523 K annealed film. The average particle size of the tiny particle was found to be ~ 20 nm which is nearly same as that of the average size as calculated from XRD data.

5 Optical properties study

5.1 Linear optical parameters

5.1.1 Transmittance (T) and Reflectance (R)

The optical transmission is the property of the film that relates transmitting power of the electromagnetic energy through it. This parameter is accounted for numerous applications

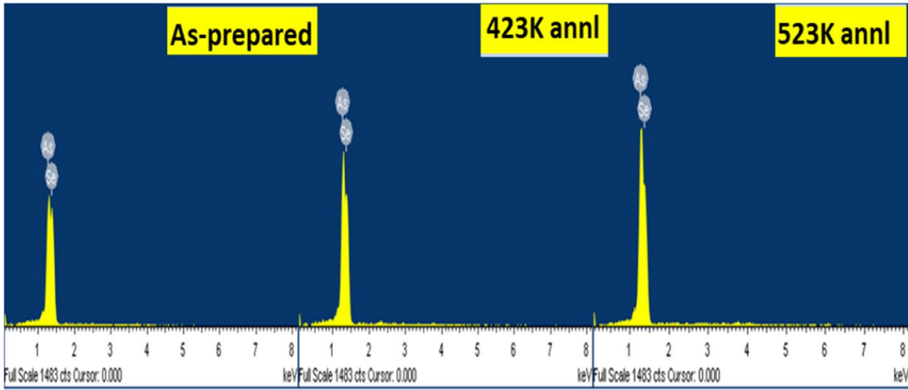

Fig. 3 EDS picture of as-prepared and annealed thin films

Table 2 Composition of as-prepared and annealed $As_{50}Se_{50}$ films

Sample	Asp-$As_{50}Se_{50}$		423 K annealed		523 K annealed	
Element	Wt.%	At. %	Wt.%	At. %	Wt.%	At. %
As L	42.65	43.94	41.95	42.32	42.28	43.01
Se L	57.35	56.06	58.05	57.68	57.62	56.99
Total	100.00	100.00	100.00	100.00	100.00	100.00

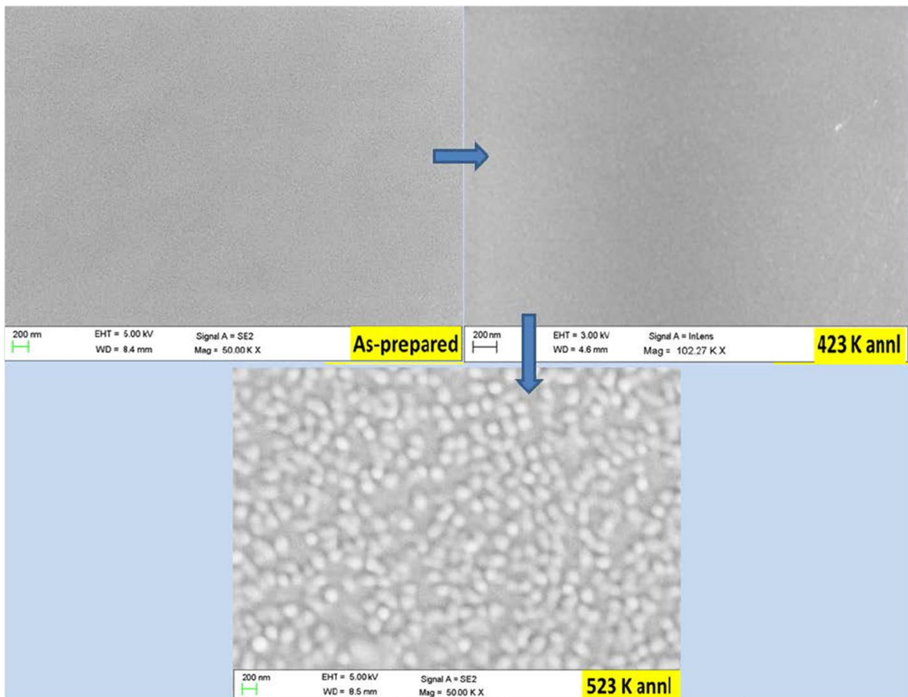

Fig. 4 FESEM picture of as-prepared and annealed thin films

in the field of optoelectronic devices. The reflectance and transmittance spectra of as-prepared and annealed films are shown in Fig. 5.

The observed oscillatory fringes in the transmission spectra over 700 nm–1150 nm wavelength range indicates the smoothness and homogeneity of the films (Naik et al. 2017). The transmittance curve could be divided into two regions (1) high absorption region of wavelength ≤ 700 nm (2) transparent region of wavelength ≥ 700 nm. The transmittance for all the films increased with wavelength but different for different films. The transmittance of the 423 K annealed film increased to a maximum value of 62% which is reduced to 59% for the 523 K annealed film.

The absorption edge shifts towards the longer wavelength side (redshift) for the 423 K annealed film whereas it shifts towards lower wavelength region (blue shift) for 523 K annealed film as compared to the as-prepared film. The reflectance of the 423 K annealed film decreased whereas it increased for the 523 K annealed film as compared to the as-prepared film. The opposite behavior in the transmittance and absorption edge for the two annealed films are in accordance with the phase transformation phenomena.

5.1.2 Absorption coefficient (α)

The absorption coefficient (α) is an important optical parameter that signifies the absorption intensity of light while passing through a material. It also has a significant relation with the bandgap and band tailing parameters of the amorphous system. It is being evaluated by using T and R values of the thin films by using the formula (Aparimita et al. 2018);

$$\alpha = \frac{1}{t} ln \frac{(1 - R)^2}{T} \tag{2}$$

where t is the thickness of the film. The behavior of α for the three thin films with wavelength is shown in Fig. 6 in which α value increased for the 523 K annealed film and

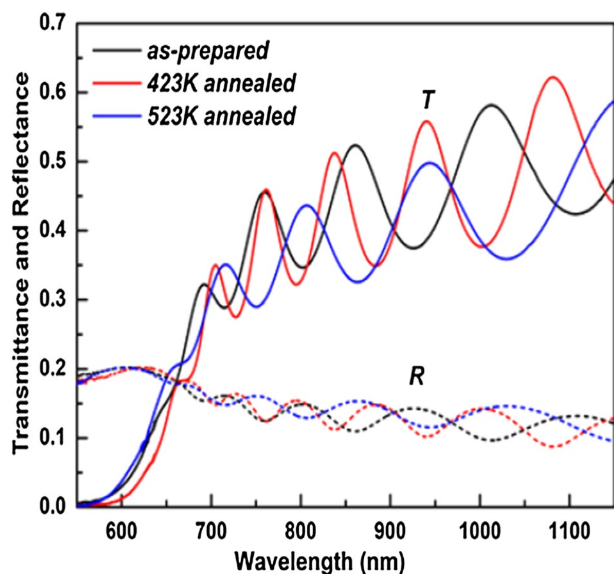

Fig. 5 T and R spectra of the studied films

decreased for the 423 K annealed film. As the film structure was converted into a crystalline one, the α value increased than that of the amorphous one (Ho et al. 2013).

5.1.3 Extinction coefficient (k)

The extinction coefficient (k) measures the loss of light that got absorbed or scattered per unit volume and also represents the material ability for polarization. The value of k was calculated from its dependence on α and λ using the relation which is given by (Behera et al. 2019);

$$k = \frac{\alpha\lambda}{4\pi} \tag{3}$$

Figure 6 (inset plot) represents the behavior of k with the energy of incident radiation ($h\nu$) which shows that the k value is more for the 523 K annealed film and less for the 423 K annealed film. Such changes in the k value leads to change in non-linear optical properties of the materials (Gad et al. 2020).

5.1.4 Optical density (OD)

The ability to absorb the electromagnetic radiation is measured by another optical parameter called as optical density which characterizes the propagation of electromagnetic radiation through the material system that can be used to manufacture several optoelectronic devices. The optical density is the product of absorption coefficient and the film thickness (Hassanien and Akl 2015).

The OD value decreased with wavelength up about 700 nm and then saturated and such abrupt decrease is almost the wavelength of absorption edges of the studied film (Fig. 7). The OD value is more for the 523 K annealed film than that of 423 K annealing which is due to the higher value of absorption coefficient.

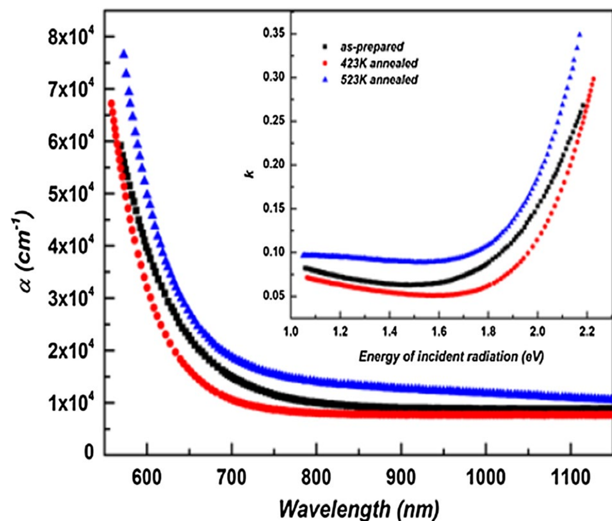

Fig. 6 α and k of the studied films

5.1.5 Skin depth (δ)

The skin depth which is also called as penetration depth (δ) is the reciprocal of absorption coefficient. This is related to the exponential behavior of the amplitude of the electromagnetic waves after overpassing the film thickness (Habubi et al. 2012). Figure 7 (inset) shows that the skin depth decreased for 523 K annealed film whereas increased for 423 K annealed film. Furthermore, the skin depth dramatically decreased near to zero value for all the films with energy of radiation. The skin depth is related to the optical bandgap (E_g) which influence the optical conductivity.

5.1.6 Optical bandgap (E_g) and Tauc parameter ($B^{1/2}$)

The optical bandgap (E_g) of the studied films was calculated by using the Tauc relation (Tauc 1974)

$$\alpha hv = B\left(hv - E_g^{Opt}\right)^m \tag{4}$$

where B represents Tauc parameter and 'm' is related to the type of electronic transition responsible for optical absorption and electron density in both valence and conduction band. The different values of 'm' such as ½, 2, 3/2 and 3 are for direct allowed, indirect allowed, direct forbidden and indirect forbidden transitions respectively (Mott and Davis 1979; Sahoo et al. 2020b). We have calculated both the direct and indirect allowed bandgap since the film structure transformed from amorphous to crystalline one.

Figure 8 represents the variations of $(\alpha hv)^{1/2}$ vs incident energy (hv) of the as-prepared and annealed thin films (inset shows $(\alpha hv)^2$ vs hv) from which energy bandgap (E_g) was obtained from the X-intercept. The direct and indirect bandgap values are presented in Table 3 which shows that the band gap decreased from 1.58 eV (as-prepared) to 1.55 eV for 423 K annealed film and increased to 1.71 eV for the 523 K annealed film. This was

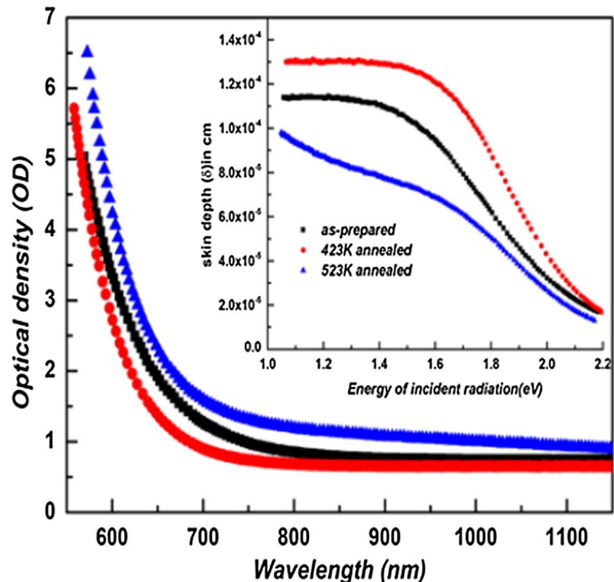

Fig. 7 Variation of OD with λ of the films

due to the amorphous to crystalline transformation after annealing above T_g. The direct bandgap values also showed similar variation in the two annealed films as compared to the as-prepared one.

The reduction of the bandgap upon annealing below T_g can be explained through the Mott and Davis model (Mott and Davis 1979). According to this model, annealing causes break down of weaker bonds to form surface dangling bonds which are responsible for the formation of localized states in the bandgap region. These localized states form band-tail, which decreases the optical bandgap like other studies due to annealing effect (Atyia and Hageb 2016; Aparimita et al. 2019). However, the increase in E_g value for the 523 K annealed film is due to the amorphous to crystalline transition that caused reduction of the defect states and increase in structural ordering as noticed from the $B^{1/2}$ values. The surface dangling bonds along with some saturated bonds were gradually annealed out by forming more heteropolar bonds than homopolar ones upon annealing at 523 K. Thus, the decrease of homopolar bonds decreased the density of localized states which consequently increased the optical bandgap (Abbady et al. 2020; Behera et al. 2017a).

The degree of disorder ($B^{1/2}$) was obtained from the slope of the fitting from Fig. 8 which is shown in Table 3. The Tauc parameter decreased for 423 K annealed film and increased for 523 K annealed film that showed the increase in structural ordering in 523 K annealed film.

5.1.7 *Urbach Energy (E_u)*

The exponential behavior of the absorption edge in the low 'α' region is represented by Urbach relation (Urbach 1953)

$$\alpha(hv) = \alpha_0 e^{\frac{hv}{E_u}} \tag{5}$$

where α_0 is a constant and E_u represents Urbach energy which was calculated from the inverse of slope from the straight-line fitting for $\ln(\alpha/\alpha_0)$ vs (hv) graph. The Urbach energy

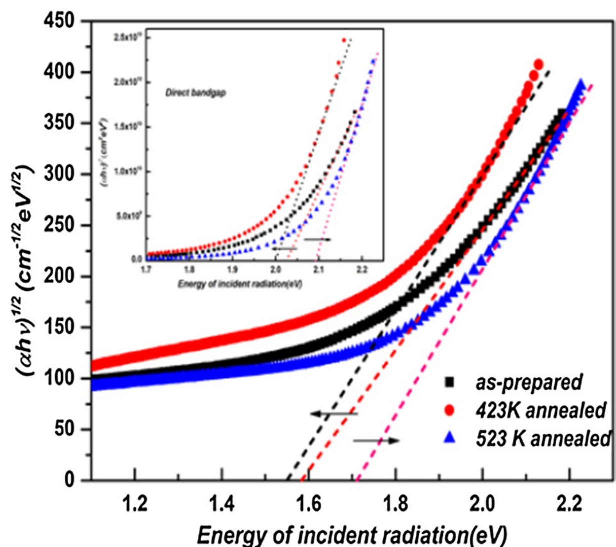

Fig. 8 Bandgap calculation for the studied films

Table 3 Optical parameters of the studied films

Optical parameters	As-prepared	423 K annealed	523 K annealed
Bandgap (E_g) eV (indirect)	1.58	1.55	1.71
Bandgap (E_g) eV (direct)	2.02	2	2.09
Tauc parameter ($B^{1/2}$) $cm^{-1/2}$ $eV^{-1/2}$	584	553	621
Urbach Energy (E_u) meV	164	183	131
Dispersion or strength energy, E_d (eV)	23.01	24.66	20.74
Single oscillator energy E_o (eV)	3.60	3.63	3.58
The first moments of the optical spectra, M_{-1}	6.391	6.793	5.793
The second moments of optical spectra, M_{-3}	0.493	0.515	0.452
Static refractive index ($n_{0)}$	2.718	2.791	2.606
High frequency dielectric constant $\varepsilon_\infty = n_0^2$	7.387	7.789	6.791
Oscillator strength $f = E_0E_d$	82.836	89.515	74.249
Dielectric constant of the lattice ($\varepsilon_{L)}$	9.05	9.33	8.34
Carrier concentration N/m*	9.36×10^{38}	7.90×10^{38}	9.47×10^{38}
Oscillator wavelength, λo (nm)	345.1	340.5	346
Oscillator strength (s_0) nm^2	5.37×10^{-5}	5.87×10^{-5}	4.83×10^{-5}
3rd order nonlinear susceptibility (χ^3) at 1.99 eV	4.22×10^{-11}	6.39×10^{-11}	2.71×10^{-11}
Nonlinear refractive index (n_2) at 1.99 eV	6.13×10^{-10}	8.61×10^{-10}	5.86×10^{-10}

measures the width of the tails of the localized states in the band gap region and also measures the degree of disorder in the film. The value of E_u is more for the 423 K annealed film and less for the 523 K annealed film (Table 3). The increase of E_u for 423 K annealed film decreased the E_g value whereas the decrease in E_u for the 523 K annealed film increased the E_g value respectively (Moustafa et al. 2019; Panda et al. 2019).

5.1.8 Linear refractive index (n)

The Swanepoel's envelope method (Swanepoel 1983) was used to estimate the first approximation refractive index (n_1) in the region of weak and moderate absorption according to the equation;

$$n_1^2 = \left[N + \left(N^2 - S^2\right)^{1/2}\right] \quad (6)$$

where $N = 2S\left(\frac{T_M - T_m}{T_M T_m}\right) + \left(\frac{S^2+1}{2}\right)$where T_m and T_M are the minima and maxima of transmittance at a particular λ and 'S' represents refractive index of glass substrate (1.51). By following the procedures as detailed in Ref.54, the actual refractive index of the films at different λ was calculated and shown in Fig. 9 (inset). In order to extract the complete behavior of 'n' for the entire wavelength region, the well-known Cauchy function $n(\lambda) = B + {}^{A}\!/_{\lambda^2}$ was used in which A and B are the Cauchy's constant. The dependence of 'n' for the entire wavelength range is shown in Fig. 9 in which decrease of n values with wavelength is attributed towards the normal dispersion of the studied films. The refractive index increased for 423 K annealed film and decreased for 523 K annealed film from the as-prepared film which is in accordance with the Moss rule i.e.,

$E_g n^4 \sim$ constant (Moss 1950) and studied by other researchers in different films (Aly et al. 2009; Behera et al. 2017b).

5.1.9 *Single oscillator energy (E_0) and Dispersion energy (E_d)*

The dispersion behavior of refractive index was studied by using the Wemple-DiDomenico (WDD) single effective oscillator model (Wemple and DiDomenico 1971) which gives an inherent physical explanation of the measured parameters by fitting the experimental data.

$$n^2 - 1 = \frac{E_0 E_d}{E_0^2 - (h\vartheta)^2} \tag{7}$$

where E_0, E_d refers to oscillator and dispersion energy respectively. Figure 10 shows the graph between $\left(n^2 - 1\right)^{-1}$ vs $(h\nu)^2$ from which the straight-line fitting gives the intercept as $\frac{E_0}{E_d}$ and slope $as(E_0 E_d)^{-1}$. The E_0 and E_d values were calculated from the slope and intercept which are given in Table 3. The E_0 is also known as an average of the energy gap that describes the information regarding the overall band structure of the system which is completely different from $E_{g.,}$ but there exists an empirical relation between E_0 and E_g, i.e. $E_0 \approx 2E_g$ (Tanaka 1980). However, in our case, the E_0 value is not exactly double of the E_g values. The dispersion energy (E_d) signifies the oscillator strength that is related to the inter band optical transition of the system. The E_0 and E_d values increased for the 423 K annealed film and decreased for the 523 K annealed film. The increase in E_o shows the increase in inter band transition whereas the increase in E_d is due to the increase of diffusion of atoms to the interstitial sites. This behavior is similar to the behavior as shown by the optical energy bandgap.

The first order and third-order moment of optical spectra i.e., M_{-1} and M_{-3} were calculated from E_0 and E_d values by using the WDD model.

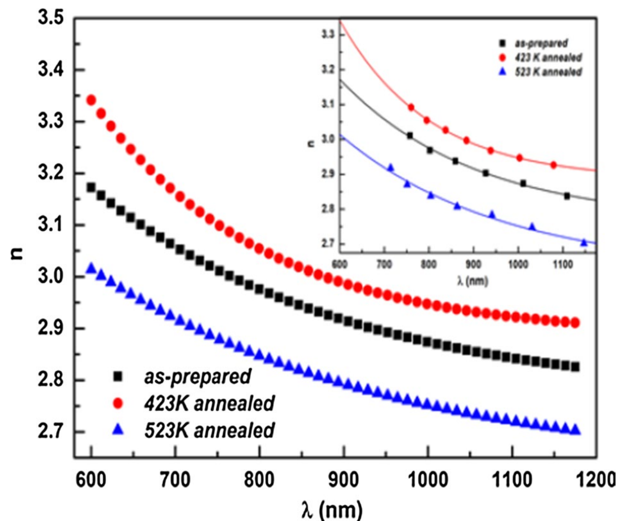

Fig. 9 n vs λ plot of the studied films

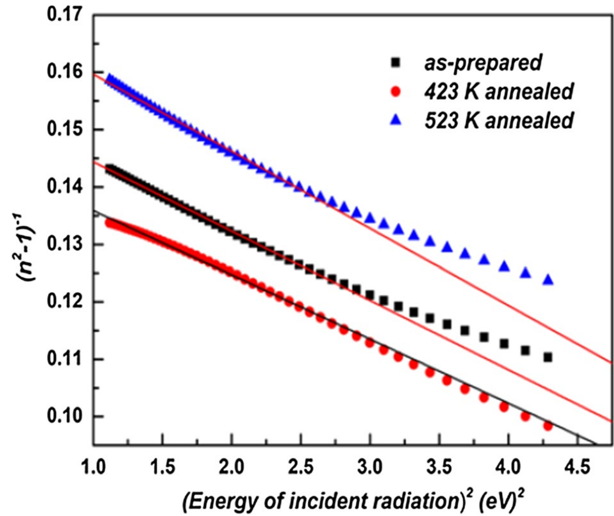

Fig. 10 $(n^2-1)^{-1}$ vs $(h\nu)^2$ of the films

$$M_{-1} = \frac{E_d}{E_0} \text{ and } M_{-3} = \frac{M_{-1}}{E_d^2} \tag{8}$$

The values of M_{-1} and M_{-3} are presented in Table 3 which infers that the moments of optical spectra increased for 423 K annealed film and then decreased for 523 K annealed film. These two optical moments are related to the effective dielectric constant and effective number of valence electrons in thin films.

The value of dielectric constant (ε_∞) as well as static refractive index (n_0) was evaluated by using the formula (Behera et al. 2019);

$$\epsilon_\infty = n_0^2 = 1 + \frac{E_d}{E_0} \tag{9}$$

The calculated ε_∞ and n_0 values for the three films are listed in Table 3 which shows the increase of these two parameters for the 423 K annealed film and decreased value for the 523 K annealed film. The oscillator strength of the films which is defined as the product of E_0 and E_d (El-Nahass et al. 2007) are presented in Table 3 that shows the increase of strength for the 423 K annealed film and decreased for 523 K annealed film.

5.2 *High-frequency dielectric constant (ε_L) and carrier concentration (N/m^*)*

The real part of dielectric constant (ε_L) and the ratio of carrier concentration per effective mass (N/m^*) were calculated by plotting n^2 with λ^2 (Fig. 11) through the given equation.

$$n^2 = \epsilon_1 = \epsilon_L - \left(\frac{e^2}{4^2 c_0^2}\right)\left(\frac{N}{m^*}\right)^2 \tag{10}$$

where ε_0 is the permittivity of free space, m^* is the effective mass of the free charge carriers and c is the velocity of light. The ε_L contributes to the polarization process inside the material (El-Nahass et al. 2014). The linear fitting gives the value of ε_L as intercept and the

value of N/m* was calculated from the slope which are presented in Table 3. The value of N/m* first decreased for 423 K annealed film and increased for 523 K annealed film. However, the ε_L value increased for 423 K annealed film and decreased for 523 K annealed film. The ε_L and N/m* depends on the internal microstructure of the films.

5.2.1 *Oscillator wavelength (λ_0) and strength of oscillator (S_0)*

The Sellmeier model for classical dispersion relation at low frequency is given by (Wemple and DiDomenico 1970),

$$(n^2 - 1)^{-1} = \frac{1}{s_0\lambda_0^2} - \frac{1}{s_0\lambda^2} \tag{11}$$

The straight-line fitting of the graph between $(n^2 - 1)^{-1}$ vs $(\lambda)^{-2}$ as shown in Fig. 12 gives $\frac{1}{s_0\lambda_0^2}$ as its Y-intercept and $\frac{1}{s_0}$ as its slope. The values of oscillator wavelength (λ_0) and oscillator strength (s_0) are shown in Table 3 which shows the opposite behavior between the two annealed films.

5.3 *Optical conductivity (σ_{opt}) and electrical conductivity (σ_{elec})*

The electronic state in the materials can be obtained from the optical conductivity (σ_{opt}) as well as electronic conductivity (σ_{elec}) which are expressed as (Abd-Elnaiem et al. 2020b),

$$\sigma_{opt} = \frac{\alpha nc}{4\pi}, \sigma_{elec} = \frac{\lambda nc}{2\pi} \tag{12}$$

The value of σ_{opt} decreased with increasing wavelength but increased with annealing temperature as shown in Fig. 13. The increase in σ_{opt} with annealing is due to the increase in absorption coefficient and increase in refractive index by thermal annealing. However, the σ_{elec} was found to be increased with wavelength and decreased with annealing temperature

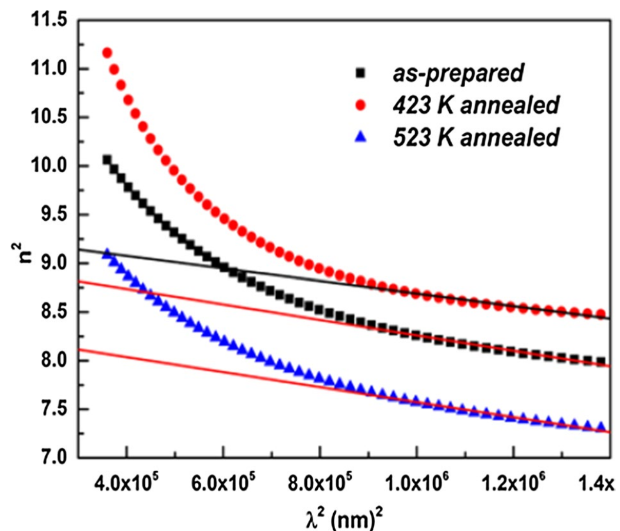

Fig. 11 n^2 vs λ^2 plot of the studied films

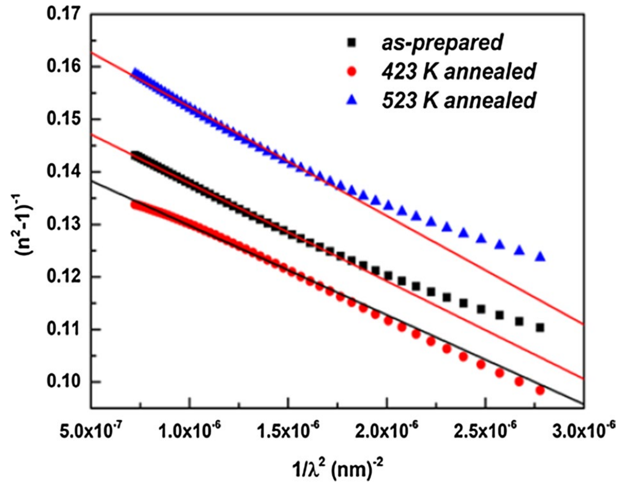

Fig. 12 $(n^2-1)^{-1}$ vs $1/\lambda^2$ plot of the studied films

(Fig. 14). The high absorption power of the 423 K annealed film is the reason for the increase in electrical conduction with decrease in optical bandgap and vice versa.

5.4 *Electrical susceptibility (χ_c)*

The electrical susceptibility is a dimensionless quantity that gives the degree of polarization of the dielectric film on application of applied electric field. This affects the electrical permittivity of the film with other phenomena like capacitance of the capacitors to the speed of light. The χ_c value is associated with the optical parameters such as 'n' and 'k' by the relation (Patterson and Bailey 2018).

$$\chi_c = \frac{1}{4\pi}\left[n^2 - k^2 - n_0^2\right] = \frac{1}{4\pi}\left[\epsilon_r - n_0^2\right] \tag{13}$$

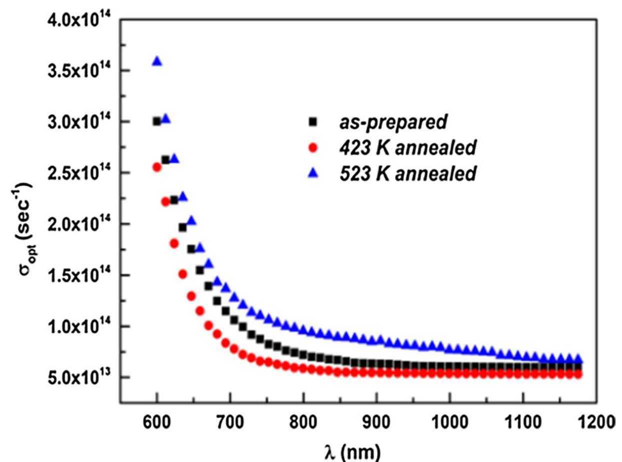

Fig. 13 Variation of optical conductivity vs λ

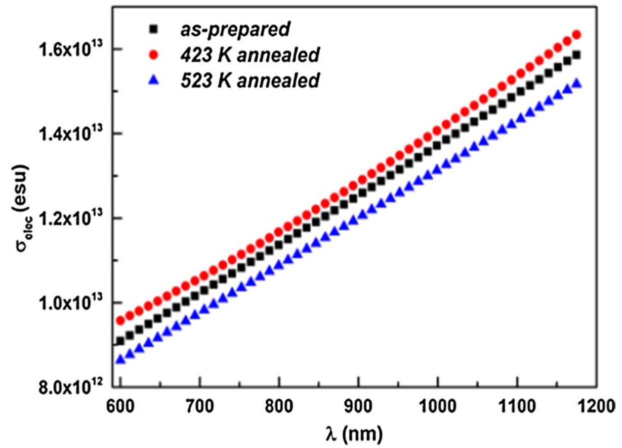

Fig. 14 Variation of electrical conductivity vs λ

The variation of χ_c value vs incident energy (hν) for the three films is shown in Fig. 15. The electrical susceptibility increased with energy value and also increased with annealing temperature. This indicates that the films under study have the ability to polarize the electric field.

5.5 Dielectric constants and loss factor

The complex dielectric function $\epsilon^* =_r +i_i$ gives the information about the dielectric properties of the solid materials. The real part (ϵ_r) measures the decrease in speed of light inside the material whereas the imaginary part (ϵ_i) measures the amount of energy absorbed in the dielectric material due to dipole motion. Overall, the parameter ϵ_r is related to dispersion, whereas ϵ_i is related to the electromagnetic wave in the dielectric medium (Tsang et al. 2004). The two parameters are related to the linear refractive index (n) and extinction coefficient (k) by the relation (Hafiz et al. 2013).

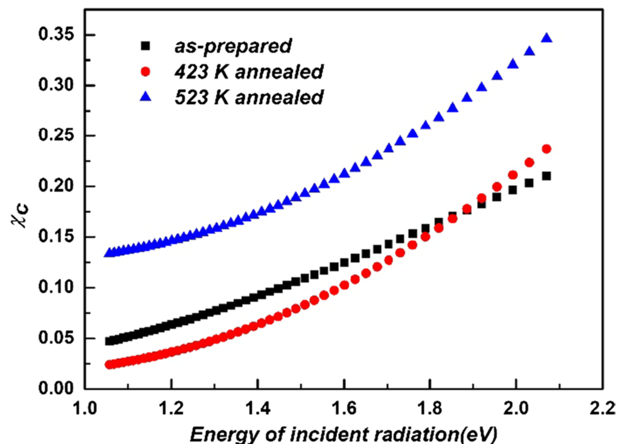

Fig. 15 Variation of χ_c vs energy of incident radiation of the three film

$$\epsilon_r = n^2 - k^2 \text{ and } \epsilon_i = 2nk \tag{14}$$

The variation of ϵ_r and ϵ_i with incident energy for different films are given in Fig. 16 (inset). The ϵ_r is more than that of the ϵ_i and the value of both the parameters increased with energy. However,ϵ_r is more for the 423 K annealed film than that of 523 K annealed film and the imaginary part showed opposite change for the two-annealing temperatures. The dielectric loss factor tan (δ) which measures the loss rate of the power of a mechanical mode is calculated by the ratio of ϵ_i to that of ϵ_r. From Fig. 17, it was observed that the loss factor increased with increasing photon energy and also increased with annealing temperature.

5.6 Non-linear optical parameters

5.6.1 *3rd order non-linear Susceptibility* ($\chi^{(3)}$)

The nonlinearity appears when there are sufficiently high intensity incident energy falls on the film which alter the properties of the system. This nonlinearity expresses itself through the polarization of the material system. Furthermore, the amorphous chalcogenide system possesses a higher value of the optical non-linear susceptibility which helps to manufacture several non-linear optical devices (Sharma et al. 2014). Ticha and Tichy (Ticha and Tichy 2002) combined the Miller's rule (Wayne 1969) with Wemple–DiDomenico single effective oscillator model for the estimation of $\chi^{(3)}$ since *Ed* and *Eo* are related to the chemistry of the material. According to Miller's principle, it can be expressed as,

$$\chi^{(3)} = \frac{A\left(n^2 - 1\right)^4}{(4\pi)^4} \tag{15}$$

where A is a constant which is equal to 1.7×10^{-10} esu. The variation of $\boldsymbol{\chi}^{(3)}$ vs hν for the three films is shown in Fig. 18 which depicts the increasing value with incident energy and the $\boldsymbol{\chi}^{(3)}$ increased for the 423 K annealed film whereas it decreased for the 523 K annealed

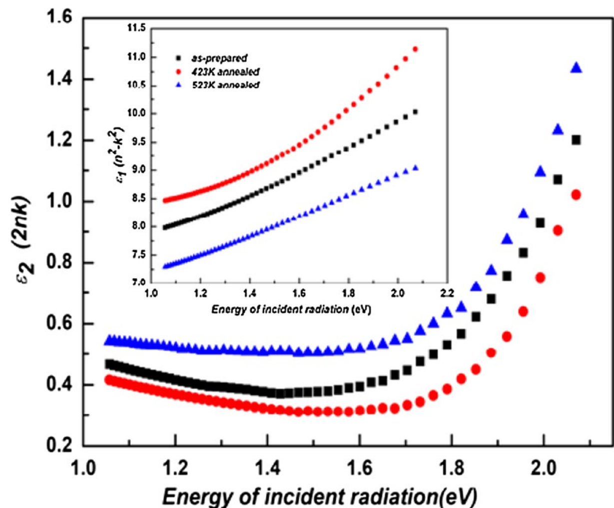

Fig. 16 Variation of ϵ_r with hν (inset ϵ_i with hν)

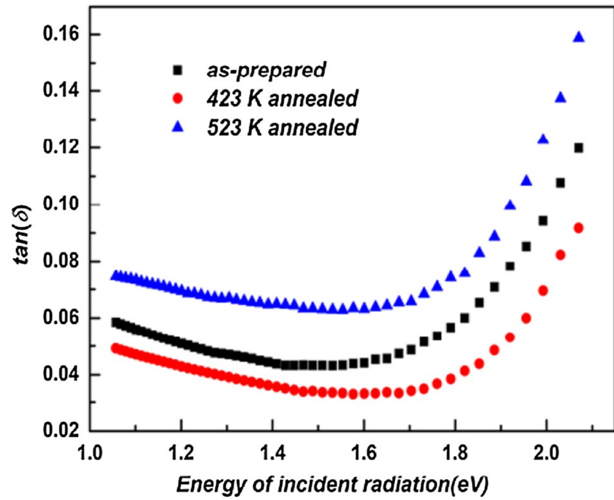

Fig. 17 Variation of tan(δ) with hν for the films

film. The calculated $\boldsymbol{\chi}^{(3)}$ values for the three films at 1.99 eV is tabulated in Table 3. Such changes in the susceptibility due to annealing can be explained by homogenization and polymerization. The presence of lone pair orbitals in chalcogenides makes them polarized easily and play an important role in nonlinear effects also (Ravindra and Srivastava 1980).

5.6.2 *Non-linear refractive index (n_2)*

According to Miller's relation, the non-linear refractive index (n_2) can be written in terms of $\chi^{(3)}$ which has the form;

$$n_2 = \frac{12\pi\chi^3}{n_0} \tag{16}$$

The obtained results are shown in Fig. 19 which indicates the increase in 'n_2' for the 423 K annealed films and decreased for 523 K annealed film like $\chi^{(3)}$ and linear refractive

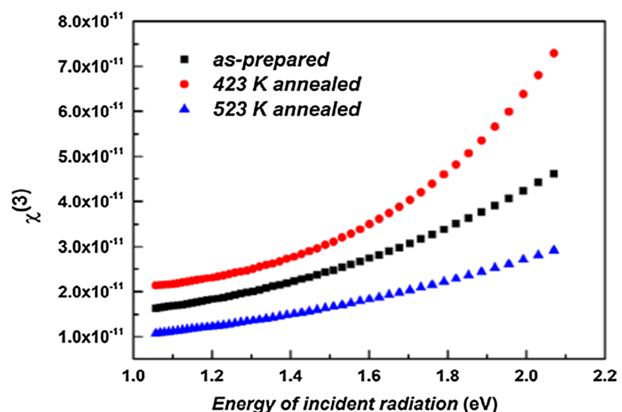

Fig. 18 Variation of $\boldsymbol{\chi}^{(3)}$ with energy of the films

index (n). This increase in nonlinearity upon annealing below T_g indicates an increase in different defect density states which can be explained through an increase in polarization of the system. The high values of non-linear parameters make these annealing induced thin films as diffraction free and suitable for non-linear devices. Due to the increase in structural order, the number of various defects in gap states decreased which leads to the reduction of nonlinearity for 523 K annealed film. The reduction of n_2 and $\chi^{(3)}$ upon annealing at 523 K can be useful for UV nonlinear materials and solid state laser(Dong et al. 2018).

6 X-ray photoelectron spectroscopy (XPS) analysis

The XPS is a surface analytic technique from which the information about different bonding can be obtained from the core-level analysis. The alterations in chemical bonding are often realized through correlation with chemical shifts in the XPS binding energies of key elements from their core-level spectra. Though the survey spectra consist of various core level and Auger spectra, we have selected the As 3d and Se 3d core level peaks for the analysis. The peak position of the As 3d core level peak for the as-prepared film was at 42.90 eV which shifted to 42.61 eV upon annealing at 423 K and to a higher value of 43.01 eV upon annealing at 523 K. Also, the intensity of the peak increased for 423 K annealed film and decreased for 523 K annealed film as compared to the as-prepared film Figs. 20 and 21

The Se $3d_{5/2}$ core level peak for the as-prepared film was at 54.61 eV which shifts to 54.73 eV upon annealing at 423 K and to a lower value of 54.48 eV upon annealing at 523 K. The $Se3d_{3/2}$ peaks which generally occurs at higher energy values than Se $3d_{5/2}$ peak is at 55.2 eV for the as-prepared film that shows shift to 55.36 eV upon 423 K annealing and to 54.87 eV upon 523 K annealing. Also, the intensity of the peak increased for 423 K annealed film and decreased for 523 K annealed film as compared to the as-prepared film. Since the electronegativity of Se (2.55) is greater than the electronegativity of As (2.18), so, the BE of Se shifts to higher values upon 423 K annealing due to the formation of more Se–Se homopolar bonds (Li et al. 2002) and the reverse change is due to the formation of more heteropolar bonds.

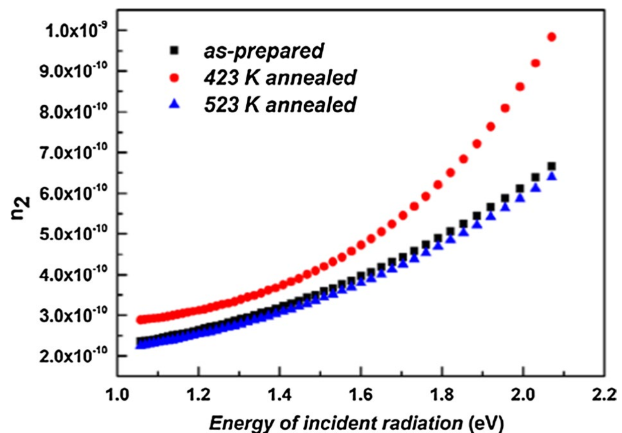

Fig. 19 Variation of n_2 with energy for the films

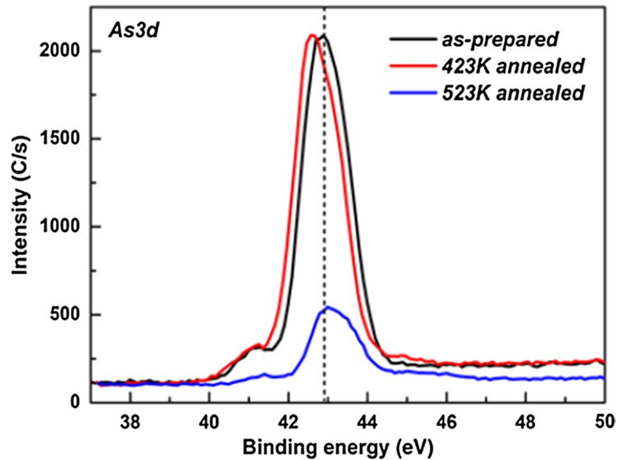

Fig. 20 As 3d core level peak of the films

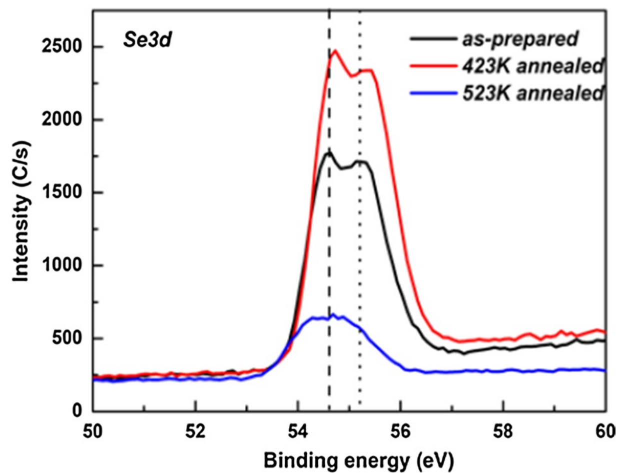

Fig. 21 Se 3d core level peak of the films

7 Conclusions

The structural transition from amorphous-crystalline upon annealing above T_g was noticed from the XRD and Raman data. The FESEM picture also showed the formation of crystallites in 523 K annealed film. Both linear and nonlinear optical parameters showed opposite changes for 423 K and 523 K annealed films. The E_g value decreased for 423 K annealed film whereas it increased for the 523 K annealed film which is discussed in terms of density of defect states and disorder value. The value of n, n_2 and $\chi^{(3)}$ increased for the 423 K annealed film and decreased for the 523 K annealed films whereas carrier concentration and oscillator wavelength showed opposite changes. The degree of disorder in the film altered as noticed from $B^{1/2}$ and E_u. The skin depth increased and optical density decreased for the 423 K annealed film which showed opposite change for the 523 K annealed film. The E_d and E_o increased for the 423 K annealed film which decreased for the 523 K annealed film. The σ_{opt} increased while σ_{elec} decreased for the 523 K annealed film while the opposite behavior was noticed for the 423 K annealed film. The χ_c was found to

be more for 523 K annealed film than that of 423 K annealed film. The real and imaginary parts of dielectric constant along with dielectric loss also showed opposite changes for the two annealed films. The XPS core level peak shifting showed the similar type of changes as that of the optical one. So, we have observed both increase and decrease in the optical parameters for the two annealed films. Such type of dual changes in the film at two different temperatures can be used for fabrication of various optical devices based on their requirement.

Acknowledgements The author Dr. Naik thank Department of Physics, Indian Institute of Science (IISc.) for Optical, XPS and Raman measurements. Dr. RD thank Department of Science and Technology, Govt. of India for Ramanujan Grant (SB/S2/RJN-075/2016).

Declarations

Conflict of interest There are no conflict of interest for this manuscript.

References

Abbady, Gh., Qasem, A., Abd-Elnaiem, A.M.: Optical parameters and electronic properties for the transition of the amorphous-crystalline phase in $Ge_{20}Te_{80}$ thin films. J. Alloys Compd. **842**, 155705 (2020)

Abd-Elnaiem, A.M., Hassan, R.M., Alamri, H.R., Assaedi, H.S.: Comparative investigation of linear and nonlinear optical properties of As–70 at % Te thin films: influence of Ga content. J. Mater. Sci. Mater. **31**, 13204–13218 (2020b)

Abd-Elnaiem, A.M., Moustafa, S., Abdelraheem, A.M., Abdel-Rahim, M.A., Mahmoud, A.Z.: Effects of annealing on structural and optical properties of $Ge_{20}Se_{70}Sn_{10}$ thin films for optoelectronic applications. J. Non-Cryst. Solids **549**, 120353 (2020a)

Adam, J.L., Zhang, X.: Chalcogenide glasses: preparation, properties and applications. Woodhead Publishing Limited, Sawston (2013)

Aly, K.A., Amer, H.H., Dahshan, A.: Optical constants of thermally evaporated Se–Sb–Te films using only their transmission spectra. Mater. Chem. Phys. **113**, 690–695 (2009)

Anne, M.L., Keirsse, J., Nazabal, V., Hyodo, K., Inoue, S., Pledel, C.B., Lhermite, H., Charrier, J., Yanakata, K., Loreal, O., Le Person, J., Colas, F., Compère, C., Bureau, B.: Chalcogenide glass optical waveguides for infrared biosensing. Sensors **9**, 7398–7411 (2009)

Aparimita, A., Sripan, C., Ganesan, R., Naik, R.: Photo and thermally induced property change in Ag diffusion into Ag/As_2Se_3 thin films. Appl. Phys. A **124**, 267 (2018)

Aparimita, A., Naik, R., Sripan, C., Ganesan, R.: Annealing induced transformations in structural and optical properties of $Ge_{30}Se_{70-x}Bi_x$ thin films. Phase Transit. **92**, 683–698 (2019)

Aparimita, A., Naik, R., Sripan, C., Ganesan, R.: Laser-induced optical photobleaching in Bi-doped $Ge_{30}Se_{70}$ amorphous thin films. Appl. Phys. A: Mater. Sci. Process. **126**, 1–8 (2020a)

Aparimita, A., Naik, R., Sahoo, S., Sripan, C., Ganesan, R.: Influence of low energy Ag ion irradiation for formation of Bi_2Se_3 phase from $Bi/GeSe_2$ heterostructure thin films. Appl. Phys. A **126**, 1–10 (2020b)

Atyia, H.E., Hageb, N.A.: Influence of thermal treatment on the optical aspects for $Ge_{20}In_5Se_{75}$ films. Optik **127**, 3888–3894 (2016)

Barr, T.L., Seal, S.: Nature of the use of adventitious carbon as a binding energy standard. J. Vac. Sci. Technol. A **13**, 1239 (1995)

Behera, M., Behera, S., Naik, R.: Optical band gap tuning by laser induced Bi diffusion into As_2Se_3 film probed by spectroscopic techniques. RSC Adv. **7**, 18428–18437 (2017a)

Behera, M., Naik, P., Panda, R., Naik, R.: Role of Te on the spectroscopic properties of $As_{50}Se_{40}Te_{10}$ thin films: An extensive study by FTIR and Raman spectroscopy. Opt. Mater. **66**, 616–622 (2017b)

Behera, M., Naik, R., Sripan, C., Ganesan, R., Mishra, N.C.: Influence of Bi content on linear and nonlinear optical properties of $As_{40}Se_{60-x}Bi_x$ chalcogenide thin films. Curr. Appl. Phys. **19**, 884–893 (2019)

Behera, M., Mishra, N.C., Khan, S.A., Naik, R.: Influence of 120 MeV Ag swift heavy ion irradiation on the optical and electronic properties of As–Se–Bi chalcogenide thin films. J. Non-Cryst. Solids **544**, 120191 (2020)

Charlie, N., Anheier, N.C., Qiao, H.A., Bernacki, B., Phillips, M.C., Petit, L., Musgraves, J.D., Richardson, K.: Measurement of the refractive index dispersion of As_2Se_3 bulk glass and thin films prior to and

after laser irradiation and annealing using prism coupling in the near and mid-infrared spectral range. Rev. Sci. Instrum. **82**, 053103 (2011)

Darwish, A.A.A., Ali, H.A.M.: On annealing induced effect in optical properties of amorphous GeSeSn chalcogenide films for optoelectronic applications. J. Alloys Compd. **710**, 431–435 (2017)

Dong, X., Huang, L., Liu, Q., Zeng, H., Lin, Z., Xu, D., Zou, G.: Perfect balance harmony in $Ba_2NO_3(OH)_3$: a beryllium-free nitrate as a UV nonlinear optical material. Chem. Commun. **54**, 5792–5795 (2018)

Eggleton, B., Luther-Davies, B., Richardson, K.: Chalcogenide photonics. Nat. Photonics **5**, 141–148 (2011)

El-Nahass, M.M., Sallam, M.M., Afifi, M.A., Zedan, I.T.: Mater. Res. Bull. **42**, 371–384 (2007)

El-Nahass, M.M., Ali, M.H., Zedan, I.T.: Photoinduced changes in linear and non-linear optical properties of $Ge_{10}In_{10}Se_{80}$ thin films. J. Non-Cryst. Solids **404**, 78–83 (2014)

Frumar, M., Frumarova, B., Wagner, T., Hrdlicka, M.: Phase change memory materials-composition, structure and properties. J. Mater. **18**, 169–174 (2007)

Gad, S.A., Shaban, H., Mansour, B.A., Mahmoud, G.M.: Determination and analysis of linear and nonlinear optical properties and electrical conductivity of amorphous $Pb_xGe_{42-x}Se_{48}Te_{10}$ thin films. Appl. Phys. A-Mater. **126**, 354 (2020)

Habubi, N.F., Oboudi, S.F., Chiad, S.S.: Study of some optical properties of mixed SnO_2–CuO thin films. J. Nano Electron. Phys. **4**, 4008 (2012)

Hafiz, M.M., Kotb, H.M., Dabban, M.A., Abdel-Latif, A.Y.: Optical properties of $Cd_{20}Se_{80-x}$Mx (M: Zn, In, and Sn) thin film alloys. Opt. Laser Technol. **49**, 188–195 (2013)

Hassanien, A.S., Akl, A.A.: Influence of composition on optical and dispersion parameters of thermally evaporated non-crystalline $Cd_{50}S_{50-x}Se_x$ thin films. J. Alloy. Comp. **648**, 280–290 (2015)

Ho, H.W., Song, W.D., Bai, K., Branicio, P.S., Tan, T.L., Ji, R., Law, L.T., Ng, C.M., Wang, L.: Correlation between optical absorption redshift and carrier density in phase changeMaterials. J. Appl. Phys. **114**, 123504 (2013)

Kalyva, M., Siokou, A., Yannopoulos, S.N., Nemec, P., Frumar, M.: Electronic and structural changes induced by irradiation or annealing in pulsed laser deposited As_{50} Se_{50} films–An XPS and UPS study. J. Phys. Chem. Solids **68**, 906–910 (2007)

Kudryashov, M., Mochalova, L., Nezdanov, A., Kornev, R., Logunov, A., Usanov, D., Mashina, A., Filpod, G.D., Gogova, D.: A novel plasma-based method for synthesis of As–Se–Te films: Impact of plasma parameters on the structure, composition, and optical properties. Superlattices Microstruct. **128**, 334–341 (2019)

Lencer, D., Salinga, M., Grabowski, B., Hickel, T., Neugebauer, J., Wuttig, M.: A map for phase-change materials. Nat. Mater. **7**, 972–977 (2008)

Li, W., Seal, S., Lopez, C., Richardson, K.A.: X-ray photoelectron spectroscopic investigation of surface chemistry of ternary As–S–Se chalcogenide glasses. J. Appl. Phys. **92**, 7102–7108 (2002)

Manivannan, R., Noyel Victoria, S.: Preparation of chalcogenide thin films using electrodeposition method for solar cell applications: a review. Sol. Energy **173**, 1144–1157 (2018)

Moss, T.S.: A relationship between the refractive index and the infra-red threshold of sensitivity for photoconductors. Proc. Phys. Soc. Sec. **63**, 167–176 (1950)

Mott, N.F., Davis, E.A.: Electronics Processes in Non-crystalline Materials, p. 428. Clarendon, Oxford (1979)

Moustafa, S., Mohamed, M., Abdel-Rahim, M.A.: Composition dependence of structural and optical properties of Ge_xSe_{100-x} semiconducting thin flms. Opt. Quant. Electron. **51**, 337 (2019)

Naik, R., Adarsh, K.V., Ganesan, R., Sangunni, K.S., Kokenyesi, S., Deshpande, U., Shripathi, T.: X-ray photoelectron spectroscopic studies on Se/As_2S_3 and Sb/As_2S_3 nanomultilayered film. J. Non-Cryst. Solids **355**, 37–42 (2009)

Naik, R., Sripan, C., Ganesan, R.: Photo darkening in $As_{50}Se_{50}$ thin film by 532nm laser irradiation. Opt. Laser Technol. **90**, 158–164 (2017)

Němec, P., Jedelský, J., Frumar, M., Štábl, M., Černošek, Z.: Structure, optical properties and their photoinduced changes in As_xSe_{100-x} (x = 50, 57.1, 60) amorphous thin films prepared by pulsed laser deposition. Thin Solid Films **484**, 140–145 (2005)

Nordman, O., Nordman, N., Peyghambarian, N.: Electron beam induced changes in the refractive index and film thickness of amorphous As_xS_{100-x} and As_xSe_{100-x} films. J. Appl. Phys. **84**, 6055–6058 (1998)

Ovshinisky, S.R., Fritzsche, H.: Amorphous semiconductors for switching memory and imaging application. IEEE Trans. Electron. Dev. **20**, 91–105 (1973)

Panda, R., Naik, R., Mishra, N.C.: Thermal annealing induced evolution of $AgIn_5Se_8$ phase from Ag/In_2Se_3 bilayer thin film. J. Alloys Comp. **778**, 819–826 (2019)

Patterson, A.L.: The Scherrer formula for X-ray particle size determination. Phys. Rev. **56**(10), 978–982 (1939)

Patterson JD, BC Bailey, 2018 Optical properties of solids, Solid-State Phys. 649–704.

Pradhan, P., Naik, R., Das, N., Panda, A.K.: Band gap tuning in $As_{40}Se_{53}Sb_{07}$ thin films by 532 nm laser irradiation: an optical investigation by spectroscopic techniques. Opt. Mater. **75**, 699–709 (2018)
Purohit, A., Chander, S., Nehra, S.P., Lal, C., Dhaka, M.S.: Effect of thickness on structural, optical, electrical and morphological properties of nanocrystalline CdSe thin films for optoelectronic applications. Opt. Mater. **47**, 345–353 (2015)
Ravindra, N.M., Srivastava, V.K.: Electronic polarizability as a function of the penn gap in semiconductors. Infrared Phys. **20**, 67–69 (1980)
Sahoo, D., Priyadarshini, P., Aparimita, A., Alagarasan, D., Ganesan, R., Varadharajaperumal, S., Naik, R.: Role of annealing temperature on optimizing the linear and nonlinear optical properties of $As_{40}Se_{50}Ge_{10}$ films. RSC Adv. **10**, 26675–26685 (2020a)
Sahoo, D., Priyadarshini, P., Dandela, R., Alagarasan, D., Ganesan, R., Varadharajaperumal, S.: Optimization of linear and nonlinear optical parameters in $As_{40}Se_{60}$ film by annealing at different temperature. Optik **219**, 165286 (2020b)
Sharma, S., Kumar, P., Thangaraj, R.: Effect of Bi additive on structure and optical properties of amorphous $Bi_xIn_{25-x}Se_{75}$ chalcogenide films. Curr. Appl. Phys. **13**, 731–735 (2013)
Sharma, I., Tripathi, S.K., Barman, P.B.: Thickness-dependent optical properties and non-linear refractive index of a-Ge–Se–In thin films. Phase Transit. **87**, 363–375 (2014)
Sharma, S., Sharma, R., Kumar, P., Thangaraj, R., Asokan, K., Mian, M.: Effect of gamma irradiation on structure and photoconductivity of amorphous $Sb_{30}Se_{70}$ chalcogenide films. J. Non-Cryst. Solids **530**, 119807 (2020)
Siokou, A., Kalyva, M., Yannopoulos, S.N., Frumar, M., Nemec, P.: Photoemission studies of As_xSe_{100-x} (x–0, 50, 100) films prepared by pulsed-laser deposition–the effect of annealing. J. Phys. Condens. Mat. **18**, 5525–5534 (2006)
Sojka, Ł, Tang, Z., Zhu, H., Bereś-Pawlik, E., Furniss, D., Seddon, A.B., Benson, T.M., Sujecki, S.: Study of mid-infrared laser action in chalcogenide rare earth doped glass with Dy^{3+}, $Pr^{3+}$and Tb^{3+}. Opt. Mater. Express **2**, 1632–1640 (2012)
Srivastava, A., Tiwari, S.N., Alvi, M.A., Khan, S.A.: Phase change studies in $Se_{85}In_{15-x}Zn_x$ chalcogenide thin films. J. Appl. Phys. **123**, 125105 (2018)
Swanepoel, R.: Determination of the thickness and optical constants of amorphous silicon. J. Phys. E: Sci Instrum. **16**, 1214–1222 (1983)
Tammama, A.K., Kahlifab, Z., Elsayed, S.A.: First and second phase transition discovery in amorphous chalcogenide Se60Te30S10 composition. J. Non-Cryst. Solids **529**, 119729 (2020)
Tanaka, K.: Optical properties and photoinduced changes in amorphous As–S films. Thin Solid Films **66**, 271–279 (1980)
Tauc, J.: Amorphous and liquid semiconductors. Plenum Press, New York (1974)
Ticha, H., Tichy, L.: Semiempirical relation between non-linear susceptibility (refractive index) linear refractive index and optical gap and its application to amorphous chalcogenides. J. Optoelectron. Adv. M. **4**, 381–386 (2002)
Tripathi, R.P., Akhtar, M.S., Alvi, M.A., Khan, S.A.: Influence of annealing treatment on phase transformation of $Ga_{15}Se_{77}T_{18}$ thin films. J. Mater. Sci. Mater. Electron **27**, 8227–8233 (2016)
Tsang, L., Kong, J.A., Ding, K.H.: Scattering of Electromagnetic Waves: Theories and Applications. Wiley, New York (2004)
Tsvetkova, T., Balabanov, S., Skordeva, E., Kitova, S., Sielanko, J., Maczka, D., Zuk, J.: Surface morphology effects of post-implantation annealing in thin amorphous films of the As–Se system. Vacuum **72**, 143–147 (2004)
Urbach, F.: The long-wavelength edge of photographic sensitivity and of the electronic absorption of solids. Phys. Rev. **92**, 1324 (1953)
Wayne, J.J.: Optical third-order mixing in Ga–As, Ge, Si, and In–As. Phys. Rev. B **178**, 1295–1303 (1969)
Wemple, S.H., DiDomenico, J.M.: Theory of the elasto-optic effect in nonmetallic crystals. Phys. Rev. B **1**, 193–202 (1970)
Wemple, S.H., DiDomenico, M.: Behavior of the electronic dielectric constant in covalent and ionic materials. Phy. Rev. B **3**, 1338–1351 (1971)
Xu, H., He, Y., Wang, X., Nie, Q., Zhang, P., Xu, T., Dai, S., Zhang, X., Tao, G.: Preparation of low-loss $Ge_{15}Ga_{10}Te_{75}$ chalcogenide glass for far-IR optics applications. Infrared Phys. Technol. **65**, 77–82 (2014)
Zakery, A., Elliott, S.R.: Optical properties and applications of chalcogenide glasses: a review. J. Non-Cryst. Solids **330**, 1–12 (2003)
Zhai, Y., Qi, R., Yuan, C., Zhang, W., Huang, Y.: High-quality chalcogenide glass waveguide fabrication by hot melt smoothing and micro-trench filling. Appl. Phys. Exp. **9**, 05220 (2016)

Zhang, W., Mazzarello, R., Wuttig, M., et al.: Designing crystallization in phase-change materials for universal memory and neuro-inspired computing. Nat. Rev. Mater. **4**, 150–168 (2019)

Zou, Y., Lin, H., Ogbuu, O., Li, L., Danto, S., Novak, S., Novak, J., Musgraves, J.D., Richardson, K., Hu, J.: Effect of annealing condition on the physio-chemical properties of spin-coated As_2Se_3 chalcogenide glass films. Opt. Mater. Exp. **2**, 1723–1732 (2012)

Publisher's Note Springer Nature remains neutral with regard to jurisdictional claims in published maps and institutional affiliations.